Engineering Analysis with Boundary Elements 104 (2019) 197–208

Contents lists available at ScienceDirect

Engineering Analysis with Boundary Elements

journal homepage: www.elsevier.com/locate/enganabound

A configurational force driven cracking particle method for modelling crack propagation in 2D

Weilong Ai[a,b], Robert E. Bird[a], William M. Coombs[a], Charles E. Augarde[a,*]

[a] Department of Engineering, Durham University, South Road, Durham DH1 3LE, UK
[b] Dyson School of Design Engineering, Imperial College London, SW7 2DB, UK

ARTICLE INFO

Keywords:
Configurational force
Cracking particle method
Meshless
Crack propagation
Computational fracture

ABSTRACT

This paper presents a novel combination of two numerical techniques to produce a method for solving fracture mechanics problems. A weak form meshless method, the cracking particles method, forms the basis of the mechanical model while crack propagation direction is calculated using configurational forces. The combined method is presented here for 2D quasi-brittle crack propagation. The configurational force approach has the advantage that it provides a prediction of the crack propagation direction which does not require decomposition of the stress and displacement fields for mixed-mode crack problems. The use of a meshless method removes the need for remeshing and it is therefore eminently suitable for multiple crack problems. The paper includes a discussion on the configurational force calculations via contour integration and domain integration and results are presented that show both approaches to be path independent when the integrations over the two crack surfaces cancel out, with domain integration generally providing better accuracy than contour integration. The contribution from the crack surfaces to the configurational force is discussed, and shown to have little influence on the final result while being easily affected by the oscillations around the crack tip. In addition, the relationship between the configurational force and the J-integral is explained. The proposed method is demonstrated on several examples, including multiple crack propagation, where good agreements with results from the literature are obtained.

1. Introduction

Crack modelling is of great importance for studying the fracture behaviour of engineering structures. Crack growth prediction involves two procedures, namely checking whether a crack will propagate and then, in which direction, with these two procedures repeated to achieve a cumulative crack propagation process. Several crack propagation criteria have been developed, some of which use the local stress and displacement fields around the crack tip, e.g. the maximum circumferential stress criterion (MCSC) in [1] and the minimum strain energy density criterion (MSEDC) in [2], while others follow a global approach based on the energy distribution throughout the cracked domain, e.g. the maximum strain energy release rate criterion (MSERRC) in [3]. These criteria have been widely used for crack modelling [4–8], and a comparison between these three criteria can be found in [9,10]. However, these criteria face issues in handling singularities caused by discontinuities and flaws, where additional physical and mathematical models (e.g. Griffith's theory of brittle fracture) are required to explain the mechanism of crack propagation.

The configurational force (CF) approach, which was first proposed by Eshelby [11], introduces the concept of a fictitious force acting on flaws in solids into the classical theory of elasticity. The CF can be interpreted as the negative gradient of the strain energy with respect to the crack tip, and provides the direction for crack advancement [12–14]. This approach has been applied to the finite element method (FEM) for brittle cracks [15–19], elastoplastic materials [20,21], 3D cracks [22], dislocations [23], crystal plasticity [24] and crack branching in dynamics [25]. Evidence of interest in the CF approach can be seen in the appearance of a recent textbook [26] and a review [21] for cracks in non-linear materials. Most recently an *r*-adaptive CF-driven crack propagation technique was developed by Miehe and co-workers [14,27] and has been extended to the discontinuous Galerkin FEM with added *p*-adaptivity [28]. Despite this recent advance, the approach has been applied with meshless methods to only a limited extent to date, and so the ease with which adaptivity can be accomplished in the latter methods has not been investigated.

Compared with the FEM, which requires elements to discretise the problem domain, meshless methods, e.g. the element free Galerkin method (EFGM) [29], the reproducing kernel particle method [30], the meshless local Petrov–Galerkin method [31] and collocation methods [32,33], use only nodal data which is convenient when modelling discontinuities and large deformation problems. Despite some differences

* Corresponding author
E-mail addresses: charles.augarde@durham.ac.uk, charles.augarde@dur.ac.uk (C.E. Augarde).

https://doi.org/10.1016/j.enganabound.2019.03.008
Received 9 December 2018; Received in revised form 10 January 2019; Accepted 5 March 2019

in the problem approximation between these methods, many similarities can be found, e.g. an absence of mesh and high order continuous shape functions, as covered in reviews [34–36]. Unlike the extended finite element method (XFEM) where crack discontinuities are described using enrichment functions [4] which bring extra unknowns and can lead to an ill-conditioned system stiffness matrix [37], meshless methods model cracks by modifying the influence domain (or "support") of particles using the visibility criterion, and therefore no extra unknowns are required [7,38]. Other alternatives for crack modelling include peridynamics [39], the numerical manifold method [40,41], the phase field method [42,43] and the cracking particle method (CPM) [44,45]. In the first of these, crack patterns are achieved by cutting "bonds" between particles so fractures are the natural outcome of this method, but problems arise as a large number of particles are needed to achieve accurate results. One attempt to improve its calculation efficiency is given in [46,47] where adaptive particle distributions are defined. The numerical manifold method uses a group of "covers" for the problem approximation and crack discontinuities are introduced by dividing these covers, but enrichments are still required for covers containing the crack tip [40]. The phase field method uses a scalar field for describing crack patterns so that tracking of crack geometries is not required, but the main issue with phase fields is the very fine mesh needed around the cracks and also an extra partial differential equation for the phase field is required, which can be computationally costly for calculating the evolution of the phase field [48]. The CPM uses a set of crack segments to describe crack paths and crack propagation is modelled through modifying these segments, which provides a simple implementation for updating crack patterns and make it therefore suitable for modelling multiple cracks [44]. Early CPMs used simple crack segments to approximate the crack patterns [49] and to model multiple cracks under impact loadings [50]. More recently the method has been extended to handle cracks with large curvatures by using bilinear segments in 2D [51] and nonplanar segments in 3D [52]. The CPM has been applied to problems including dynamic fracture [53], ductile fracture [54,55], shear bands [56] and multiple cracks [57].

In this paper, the CPM is developed further to incorporate the CF approach for crack propagation, making use of the advantages of the two methods, the first time that this has been attemptted to the authors' knowledge. The CPM provides a simple description of crack discontinuities, and the CF approach has a simpler implementation than the MCSC, which has already been used in the CPM [51] for predicting crack propagation direction. This paper is structured as follows. The theories of the CPM and the CF are introduced in Sections 2 and 3, respectively. The implementation of the CF into the CPM is also included in Section 3, where both contour integration and domain integration for calculating the CF are covered. Several numerical examples are used to demonstrate the performance of the proposed method in Section 4, which is followed by a summary of the paper in Section 5.

2. Cracking particle method

The CPM, developed in [44,50,51], is based on the weak-form based EFGM [29] for problem discretisation and is focused on fracture problems. This method is meshless and uses only nodal data to discretise the problem domain, so no remeshing is required for crack modelling. The governing equations for the quasi-static behaviour of elastic isotropic materials in 2D and the associated weak form in the EFGM have been covered by many papers [29,50,51] and will not be repeated here, however details of the means by which crack discontinuities are handled have not been covered in detail before and are included below to demonstrate the key features of the CPM.

2.1. Moving least squares approximation

The displacement field is modelled, as in [29], by a moving least squares (MLS) approximation, as

$$u^h(\mathbf{x}) = \sum_{i=1}^{n} \Phi_i(\mathbf{x}) u_i = \mathbf{\Phi}^{\mathrm{T}} \mathbf{u}, \tag{1}$$

where u^h is the approximated displacement, u_i is the nodal value of displacement at the ith node, $\mathbf{x}$ is the coordinate vector with $\mathbf{x} = [x_1, x_2]$ in 2D, n is the number of nodes with influence domains covering $\mathbf{x}$, Φ_i is ith shape function calculated by the MLS approximation, $\mathbf{u}$ and $\mathbf{\Phi}$ are vectors of u_i and Φ_i, respectively, for n nodes. The shape function $\mathbf{\Phi}$ is obtained as in [29] by

$$\mathbf{\Phi}(\mathbf{x}) = \mathbf{p}^{\mathrm{T}}(\mathbf{x}) \mathbf{A}^{-1}(\mathbf{x}) \mathbf{B}(\mathbf{x}), \tag{2a}$$

$$\mathbf{A}(\mathbf{x}) = \sum_{i}^{n} w_i(\mathbf{x}) \mathbf{p}^{\mathrm{T}}(\mathbf{x}_i) \mathbf{p}(\mathbf{x}_i), \tag{2b}$$

$$\mathbf{B}(\mathbf{x}) = [w_1(\mathbf{x})\mathbf{p}(\mathbf{x}_1), w_2(\mathbf{x})\mathbf{p}(\mathbf{x}_2) \dots w_n(\mathbf{x})\mathbf{p}(\mathbf{x}_n)], \tag{2c}$$

where $\mathbf{p}(\mathbf{x})$ is the basis function, e.g. $\mathbf{p}(\mathbf{x}) = [1, x_1, x_2]^{\mathrm{T}}$ for a linear basis in 2D, and w is a weight function, e.g. the 4th order spline function adopted in this paper

$$w_i(\mathbf{x}) = w(r) = \begin{cases} 1 - 6r^2 + 8r^3 - 3r^4 & \text{if } r \le 1, \\ 0 & \text{if } r > 1, \end{cases} \tag{3}$$

where $r = \|\mathbf{x} - \mathbf{x}_i\| / r_i$, and r_i is the radius of a circular influence domain (support) of the ith particle, while $\|\cdot\|$ stands for the L_2 norm. Different weight functions and support sizes for the above are discussed in [58], indicating that both can affect the error of the MLS approximation, however this error is problem-dependent and convergent results can usually be obtained. The support size is defined as a factor d_s multiplying the average nodal spacing, where d_s is suggested in the range between 2.0 and 4.0 [59]. Here, $d_s = 2.2$ is used for all examples in Section 4.

2.2. Crack modelling

In the CPM, crack paths are approximated with a set of segments centred at particles. There are two steps in the development of the CPM for handling crack discontinuities, using extrinsic enrichment [44,60] or intrinsic enrichment [50,51]. The former introduces some discontinuous enrichment functions into the displacement polynomial approximation (named extrinsic enrichment) where extra unknowns are involved which can however make the global stiffness matrix ill-conditioned, similar to issues met with the XFEM [37]. The latter divides the influence domain of particles using the visibility criterion, and no extra unknowns are introduced in the MLS approximation, and is therefore called intrinsic enrichment.

Here, intrinsic enrichment is used in the problem approximation. Instead of straight segments in the original CPM [44], bilinear crack segments first presented in [51] are employed for representing crack paths, which can provide a better description of crack patterns, as illustrated in Fig. 1. The angular change in a crack path is captured by these bilinear crack segments, so a nearly continuous crack path can be achieved. Crack opening, marked with the operator $[[\cdot]]$, is obtained from the relative displacement between particles on the two sides of the crack,

$$[\![u(\mathbf{x})]\!] = \sum_{i \in S^+} \Phi_i(\mathbf{x}^+) u_i - \sum_{i \in S^-} \Phi_i(\mathbf{x}^-) u_i, \tag{4}$$

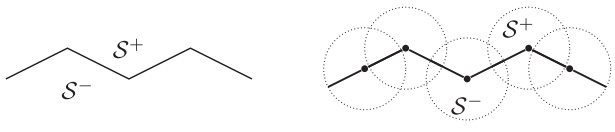

(a) crack (b) modelling

Fig. 1. Crack modelling in the cracking particle method: (a) crack path and (b) crack segments, with dashed circles indicating the influence domain of particles.

where S^+ and S^- indicate the two sides of the crack. An *h*-adaptivity approach has also been introduced into the CPM in [51] to maintain calculation efficiency and to handle the high stress gradients around the crack tip, details of which are given here in Appendix A. Since shape functions of the MLS approximation do not possess the Kronecker delta property, essential boundary conditions cannot be imposed directly but through Lagrange multipliers as in [29,51].

3. Configurational force

The classical theory of elasticity faces issues in handling the concept of forces acting on singularities (cracks or concave corners). This issue was addressed by Eshelby [11] through the CF theory. The CF is regarded as the negative gradient of the potential energy with respect to a singularity, which represents the energy change at the singularity for solids undergoing deformation [11]. The potential energy is measured by the Eshelby stress tensor $\boldsymbol{\Sigma}$ defined as

$$\boldsymbol{\Sigma} = W\boldsymbol{\delta} - \mathbf{H}^{\mathrm{T}} \cdot \boldsymbol{\sigma}, \tag{5}$$

where $\boldsymbol{\delta}$ is an identity matrix (2×2 in 2D), $\mathbf{H}$ is the displacement gradient tensor with components $H_{ij} = \partial u_i/\partial x_j$, W is the strain energy, $W = \frac{1}{2}\sigma_{ij}\partial u_i/\partial x_j$ and indexes are defined with Einstein summation, $\boldsymbol{\sigma}$ is the Cauchy stress and σ_{ij} is a component. Similar to the equilibrium of Cauchy stress for a continuum, the Eshelby stress $\boldsymbol{\Sigma}$ is also self-equilibrating, as

$$\nabla \cdot \boldsymbol{\Sigma} = \mathbf{0} \quad \text{in } \Omega. \tag{6}$$

Integrating Eq. (6) over a simply connected domain and using Green's theorem (the 2D version of the divergence theorem), the resultant of the Eshelby stress for a contour path Γ encircling the domain must vanish, as

$$\oint_{\Gamma} \boldsymbol{\Sigma} \cdot \mathbf{n}\, \mathrm{d}\Gamma = \mathbf{0}, \tag{7}$$

where $\mathbf{0}$ is a zero vector and $\mathbf{n}$ is the outward normal to Γ. If the problem domain contains a crack, as illustrated in Fig. 2, the resultant from Eq. (7) is nonzero. The CF at the crack tip $\mathbf{g}$ is obtained by integrating over an infinitesimal contour C_s [14,27], as

$$\mathbf{g} = \lim_{|C_s|\to 0} \int_{C_s} \boldsymbol{\Sigma} \cdot \mathbf{n}\, \mathrm{d}\Gamma, \tag{8}$$

where $\mathbf{g}$ is a vector of fictitious forces, e.g. $\mathbf{g} = [g_1, g_2]$ in 2D. The CF is related to a body's material structures, performs work when these structures evolve in the process of, for instance, phase transition at interfaces or crack propagation, and provides a pictorial description of the body's response to these evolutions [61].

3.1. Implementation in the CPM

Here the CF is implemented into the CPM for crack modelling. Since the stress distribution is singular at the crack tip in linear elastic fracture mechanics, it is not appropriate to use the results at the crack tip directly.

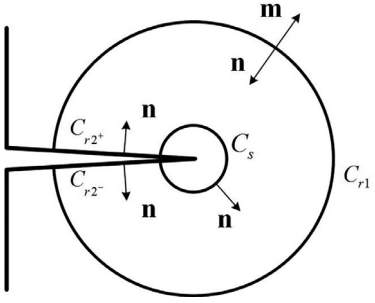

Fig. 2. Integration path around the crack tip.

Eq. (8) is therefore modified to an integration over a contour away from the crack tip, as

$$\int_{C_s} \boldsymbol{\Sigma} \cdot \mathbf{n}\mathrm{d}\Gamma = \oint_{C} \boldsymbol{\Sigma} \cdot \mathbf{n}\mathrm{d}\Gamma - \int_{C_{r2}} \boldsymbol{\Sigma} \cdot \mathbf{n}\mathrm{d}\Gamma - \int_{C_{r1}} \boldsymbol{\Sigma} \cdot \mathbf{n}\mathrm{d}\Gamma, \tag{9}$$

where $C = C_s + C_{r1} + C_{r2}$ is a closed contour with $C_{r2} = C_{r2^-} + C_{r2^+}$ as depicted in Fig. 2. Using Eq. (7), the first term on the right hand side (*r.h.s.*) of Eq. (9) becomes zero. With the definition of the Eshelby stress in Eq. (5), the second term on the *r.h.s.* of Eq. (9) is

$$\int_{C_{r2}} \boldsymbol{\Sigma} \cdot \mathbf{n}\mathrm{d}\Gamma = \int_{C_{r2}} (W\boldsymbol{\delta} \cdot \mathbf{n} - \mathbf{H}^{\mathrm{T}} \cdot \boldsymbol{\sigma} \cdot \mathbf{n})\mathrm{d}\Gamma. \tag{10}$$

The crack surfaces are assumed traction-free, as $\boldsymbol{\sigma} \cdot \mathbf{n} = \mathbf{0}$ on the crack surfaces C_{r2}. For C_{r2^-} and C_{r2^+}, their normals are reversed so these two parts are sometimes excluded from the calculation of the CF when the difference of strain energy between the two sides of crack surfaces is neglected, e.g. [27], as

$$\int_{C_{r2}} \boldsymbol{\Sigma} \cdot \mathbf{n}\mathrm{d}\Gamma = \int_{C_{r2}} W\boldsymbol{\delta} \cdot \mathbf{n}\mathrm{d}\Gamma \approx 0. \tag{11}$$

The CF by contour integration therefore becomes

$$\mathbf{g} = -\int_{C_{r1}} \boldsymbol{\Sigma} \cdot \mathbf{n}\mathrm{d}\Gamma. \tag{12}$$

Alternatively, a domain integral can be used to calculate the CF. To set up an integral over a closed contour path as in [19], Eq. (8) is adjusted to

$$\int_{C_s} \boldsymbol{\Sigma} \cdot \mathbf{n}\mathrm{d}\Gamma = \oint_{C} q(\mathbf{x})\boldsymbol{\Sigma} \cdot \mathbf{n}\mathrm{d}\Gamma - \int_{C_{r2}} q(\mathbf{x})\boldsymbol{\Sigma} \cdot \mathbf{n}\mathrm{d}\Gamma, \tag{13}$$

where $q(\mathbf{x})$ is a weight function which should satisfy

$$q(\mathbf{x}) = \begin{cases} 1 & \text{on } C_s \\ 0 & \text{on } C_{r1} \\ \text{arbitrary} & \text{within } \Omega_{\mathrm{c}}, \end{cases} \tag{14}$$

The first term on the *r.h.s.* of Eq. (13) can be converted to a domain integral using Green's theorem, as

$$\oint_{C} q(\mathbf{x})\boldsymbol{\Sigma} \cdot \mathbf{n}\mathrm{d}\Gamma = -\oint_{C} q(\mathbf{x})\boldsymbol{\Sigma} \cdot \mathbf{m}\mathrm{d}\Gamma = -\int_{\Omega_{\mathrm{c}}} \nabla\Big(q(\mathbf{x})\boldsymbol{\Sigma}\Big)\mathrm{d}\Omega_{\mathrm{c}}, \tag{15}$$

where $\mathbf{m}$ is the outward normal to the contour C_{r1} and Ω_{c} is the domain encircled by the contour C. When $\lim C_s \to 0$ and C_{r2} approaches the crack surfaces, Ω_{c} can be regarded as the domain encircled by C_{r1}. Substituting Eq. (6) into Eq. (15) yields

$$-\int_{\Omega_{\mathrm{c}}} \nabla\big(q(\mathbf{x})\boldsymbol{\Sigma}\big)\mathrm{d}\Omega_{\mathrm{c}} = -\int_{\Omega_{\mathrm{c}}} \boldsymbol{\Sigma} \cdot \nabla q(\mathbf{x})\mathrm{d}\Omega_{\mathrm{c}}. \tag{16}$$

The second term on the *r.h.s.* of Eq. (13) is not considered in [14,27], but is included in [19]. A discussion on this issue, i.e. whether to include the integration over crack surfaces for the CF, will be given later. Without integrating over crack surfaces, the final domain integration for the CF becomes

$$\mathbf{g} = -\int_{\Omega_{\mathrm{c}}} \boldsymbol{\Sigma} \cdot \nabla q(\mathbf{x})\mathrm{d}\Omega_{\mathrm{c}}. \tag{17}$$

It is notable that the domain integration in Eq. (17) is path-independent when the crack surface terms cancel out, so the CF can be calculated using the stress and displacement fields away from the crack tip. The implementation for calculating the CF in the CPM is not complicated. After a solution for the stress and displacement fields is obtained, the CF is calculated by Eq. (17) through a post-processing procedure. The integration uses a Gauss quadrature scheme over a square domain Ω_{c} centred at the crack tip as shown in Fig. 3. Eq. (17) is consistent with Miehe's solution [14,27] for calculating the CF in the FEM, when doing the integration over the elements containing the crack tip and replacing the weight function $q(\mathbf{x})$ with the shape function of the crack tip, i.e. $q(\mathbf{x}) = N(\mathbf{x})$.

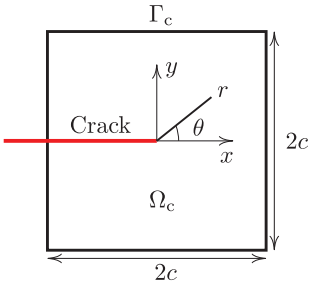

Fig. 3. Integration domain around the crack tip.

3.2. Crack propagation

Different crack propagation criteria have been developed to model fracture behaviour in brittle materials including the MCSC, the MSEDC and the MSERRC, e.g. in [9,10]. The MCSC has been used in the CPM [51,52] for its simplicity and accuracy over the other two methods [9], while the CF is another alternative and has a simpler implementation as in [22,28]. In the MCSC, a crack propagates towards the direction where the shear stress at the crack tip is zero, as detailed in Appendix B, and the shear stress is represented by SIFs to avoid the issue of stress singularity at the crack tip. SIFs are calculated using the interaction integral in Appendix C, which requires the decomposition of the stress and displacement fields with respect to the crack for mixed mode crack problems. In contrast, the use of the CF can be regarded as more elegant since this decomposition is not required in the calculation of Eq. (17), and the crack propagation direction is directly provided by the CF. The vector $\mathbf{g}$ provides the crack propagation direction and determines whether the crack can propagate, e.g. crack propagation occurs when $\|\mathbf{g}\|$ (the L_2 norm of $\mathbf{g}$) exceeds g_c, where g_c is the critical energy release per unit area of crack surface. Having determined direction, a constant increment of crack extension da is given to the crack as in [14], which is proportional to the initial crack length a and will be specified in numerical examples in Section 4. If the angular change of crack direction is larger than 5°, the crack increment is reduced to 0.5da, by which the accuracy in predicting the curvature of crack growth is ensured. The position of the new tip is obtained using the CF as demonstrated in Fig. 4, and if there is no particle at this location, a new cracking particle is created, otherwise the particle located at this position is cracked. A successive crack propagation process can be achieved by duplicating these procedures. Note that special handling is required in the FEM, e.g. dividing elements for crack growth [19] and relocating element edges in [14], which is not necessary in the CPM due to its meshless nature.

It is more common to use the J-integral in fracture mechanics for modelling crack propagation, but the CF provides another option and it is worth demonstrating the relationship between the CF and the J-integral here. The J-integral can be regarded as the projection of the CF to the crack extension direction $\mathbf{e}$ as mentioned in [62], that is

$$J = \mathbf{e}\cdot\mathbf{g} = -\lim_{|C_s|\to 0}\int_{C_s}\mathbf{e}\cdot\boldsymbol{\Sigma}\cdot\mathbf{n}\mathrm{d}\Gamma. \tag{18}$$

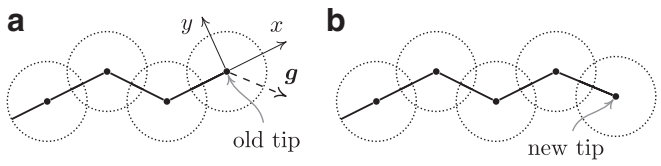

Fig. 4. Crack propagation driven by the configurational force in the cracking particle method: (a) configurational force in the local coordinate system and (b) new crack tip.

The relationship between the J-integral and the stress intensity factors (SIFs) K_I and K_II is

$$J = \alpha(K_\mathrm{I}^2 + K_\mathrm{II}^2), \tag{19}$$

and

$$\alpha = \begin{cases} (1-\nu^2)/E & \text{for plane strain,} \\ 1/E & \text{for plane stress.} \end{cases} \tag{20}$$

Alternatively the CF has a relationship with the SIFs [63] as

$$g_1 = J = \alpha({K_\mathrm{I}}^2 + {K_\mathrm{II}}^2), \tag{21a}$$

$$g_2 = -2\alpha K_\mathrm{I} K_\mathrm{II}. \tag{21b}$$

4. Numerical examples

Four 2D numerical examples are used to demonstrate the performance of the proposed method, and a comparison between the CF and the MCSC (using the J-integral) in modelling crack propagation is included. All problems are assumed to have plane stress conditions and linear elastic isotropic material properties except in Sections 4.2 and 4.4 where plane strain conditions are used. The CF is calculated by the contour integration in Eq. (12) over the path Γ_c in Fig. 3 and the domain integration in Eq. (17) over the area Ω_c encircled by Γ_c. The contour Γ_c is a square with dimensions of $2c\times 2c$ centred at the crack tip, and c is proportional to the initial crack length a, as specified later. The weight function $q(\mathbf{x})$ is taken to be a simple bi-linear expression with the form

$$q(\mathbf{x}) = \left(1-\frac{x}{c}\right)\left(1-\frac{y}{c}\right), \tag{22}$$

where x and y are local coordinates at the crack tip, as shown in Fig. 3, which are parallel and normal to the crack surface, respectively. A large number of Gauss points are used to ensure the accuracy of integration around the crack tip with high stress gradients. For the contour integration, each edge of Γ_c is divided into 6 segments, each with 8 Gauss quadrature points, while the domain integration is calculated with 6×6 background cells each with 8×8 Gauss quadrature points. The SIFs are obtained by the interaction integration over the domain Ω_c with the same Gauss quadrature scheme. For easy data analysis, the following normalisation is used for the CF and the SIFs, as

$$J' = \frac{J}{\alpha\sigma^2\pi a}, \quad \mathbf{g}' = \frac{\mathbf{g}}{\alpha\sigma^2\pi a}, \tag{23a}$$

$$K_\mathrm{I}' = \frac{K_\mathrm{I}}{\sigma\sqrt{\pi a}}, \quad K_\mathrm{II}' = \frac{K_\mathrm{II}}{\sigma\sqrt{\pi a}}, \tag{23b}$$

where σ is a measure of the external loading and a is the initial crack length.

4.1. Half central crack

The half central crack problem in [57] is the first problem to be analysed, as shown in Fig. 5. This example is extracted from the problem of a central crack in an infinite plate subjected to far field stress. The dimensions are plate length $w = 100$ mm, crack length $a = 0.5w$ and target error (see Appendix A) for adaptivity $\eta_\mathrm{t} = 0.02$. Two situations, pure mode I and mixed mode fracture, are included to study the contribution from crack surfaces to the CF, considering that the deformation in pure mode I fracture is symmetric and for mixed mode fracture it is not. An analytical solution for this problem is provided by [64]

$$\sigma_{11} = \frac{K_\mathrm{I}}{\sqrt{2\pi r}}\cos\left(\frac{\theta}{2}\right)\left[1-\sin\left(\frac{\theta}{2}\right)\sin\left(\frac{3\theta}{2}\right)\right] - \frac{K_\mathrm{II}}{\sqrt{2\pi r}}\sin\left(\frac{\theta}{2}\right)\left[2+\cos\left(\frac{\theta}{2}\right)\cos\left(\frac{3\theta}{2}\right)\right], \tag{24a}$$

Table 1
Mode I fracture for a half central crack (analytical values $K'_{\mathrm{I}} = 1$, $K'_{\mathrm{II}} = 0$).

	Configurational force								
	Contour integration		Domain integration		Crack surface part		J-integral		
c/a	g'_1	g'_2	g'_1	g'_2	g'_1	g'_2	K'_{I}	K'_{II}	J'
0.5	1.0038	0.0000	1.0017	0.0000	0.0000	0.0000	1.0011	0.0000	1.0011
0.1	0.9992	0.0000	1.0040	0.0000	0.0000	0.0000	1.0026	0.0000	1.0026
0.01	1.0025	0.0000	0.9812	0.0000	0.0000	0.0000	0.9901	0.0000	0.9901
0.001	0.9837	0.0000	0.8496	0.0000	0.0000	0.0000	0.9091	0.0000	0.9091

Table 2
Mixed mode fracture for a half central crack (analytical values $K'_{\mathrm{I}} = 1$, $K'_{\mathrm{II}} = 1$).

	Configurational force								
	Contour integration		Domain integration		Crack surface part		J-integral		
c/a	g'_1	g'_2	g'_1	g'_2	g'_1	g'_2	K'_{I}	K'_{II}	J'
0.5	1.9940	−1.9963	1.9994	−2.0003	0.0000	−0.0178	0.9999	1.0001	2.0001
0.1	2.0033	−2.0033	1.9987	−2.0019	0.0000	−0.0211	0.9999	0.9999	1.9995
0.01	2.0076	−2.0026	1.9910	−1.9999	0.0000	−0.1710	0.9973	0.9986	1.9918
0.001	2.0043	−1.9873	1.9883	−1.9927	0.0000	0.1256	0.9947	0.9994	1.9882

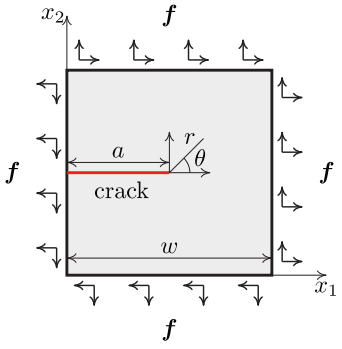

Fig. 5. The configuration of an half central crack in a square plate.

$$\sigma_{22} = \frac{K_{\mathrm{I}}}{\sqrt{2\pi r}} \cos\left(\frac{\theta}{2}\right)\left[1 + \sin(\frac{\theta}{2}) \sin\left(\frac{3\theta}{2}\right)\right] + \frac{K_{\mathrm{II}}}{\sqrt{2\pi r}} \sin\left(\frac{\theta}{2}\right) \cos\left(\frac{\theta}{2}\right) \cos\left(\frac{3\theta}{2}\right), \tag{24b}$$

$$\sigma_{12} = \frac{K_{\mathrm{I}}}{\sqrt{2\pi r}} \cos\left(\frac{\theta}{2}\right) \sin\left(\frac{\theta}{2}\right) \cos\left(\frac{3\theta}{2}\right) + \frac{K_{\mathrm{II}}}{\sqrt{2\pi r}} \cos\left(\frac{\theta}{2}\right)\left[1 - \sin\left(\frac{\theta}{2}\right) \sin\left(\frac{3\theta}{2}\right)\right]. \tag{24c}$$

The stresses from Eq. (24) along four edges of the plate are used as the external loading, as

$$\bar{\mathbf{t}} = \boldsymbol{\sigma} \cdot \mathbf{n} = [\sigma_{11} n_1 + \sigma_{12} n_2,\ \sigma_{12} n_1 + \sigma_{22} n_2]^{\mathrm{T}}, \tag{25}$$

and the plate is fixed against rigid body movement using the following constraints,

$$u_1 = 0, u_2 = 0 \quad \text{at } x_1 = w/2, x_2 = w/2, \tag{26a}$$

$$u_2^{S^+} + u_2^{S^-} = 0 \quad \text{at } x_1 = 0, x_2 = w/2, \tag{26b}$$

where superscripts S^+ and S^- are as depicted in Fig. 1. Pure mode I and mixed mode fractures were obtained by setting different types of external loading $\bar{\mathbf{t}}$ using $K'_{\mathrm{I}} = 1$, $K'_{\mathrm{II}} = 0$ and $K'_{\mathrm{I}} = 1$, $K'_{\mathrm{II}} = 1$, respectively.

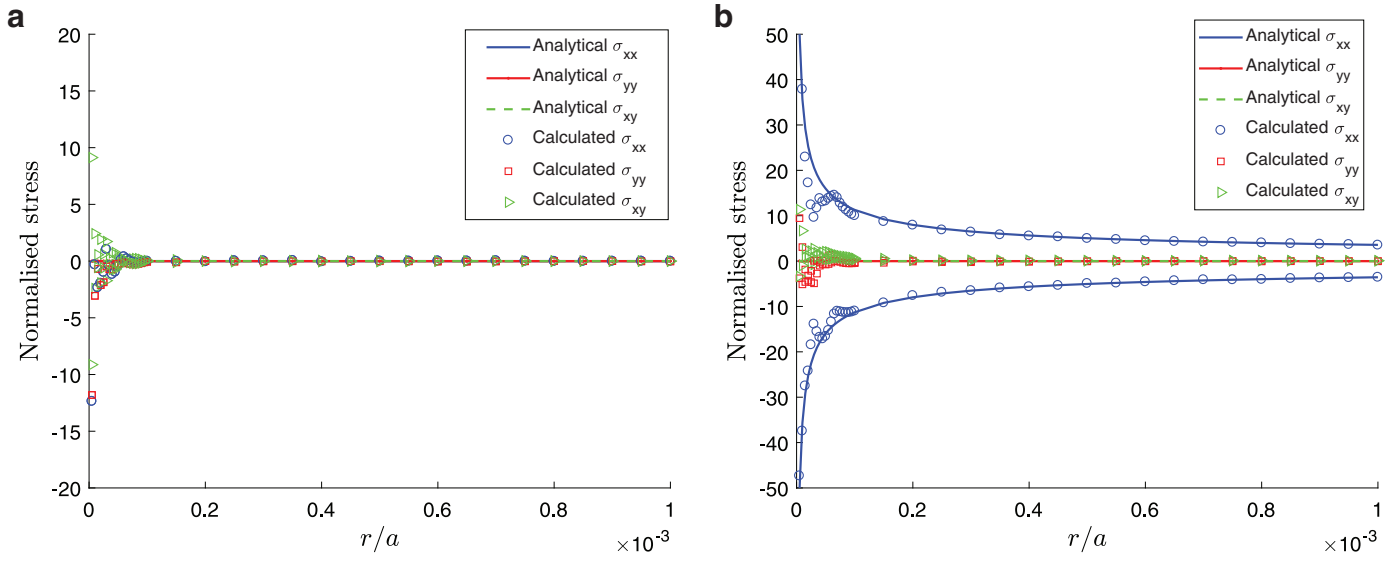

Fig. 6. Stresses along the crack surfaces for the half central crack problem: (a) mode I and (b) mixed mode.

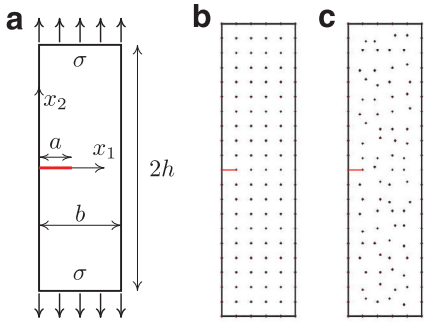

Fig. 7. Single edge crack in a slender plate under tensile loading: (a) configuration; (b) case 1 and (c) case 2.

The calculation of the CF was through either the contour integration in Eq. (12) or the domain integration in Eq. (17), where the contribution from crack surfaces was calculated using the second term on the *r.h.s.* of Eq. (13), over various sizes of contours and domains e.g. $c/a = 0.001, 0.01, 0.1, 0.5$. The SIFs were obtained by the interaction integration as in Appendix C,

The initial particle arrangement was set at 21×21 uniformly distributed particles, and then the adaptivity approach including 12 adaptive steps was used to modify the particle arrangements. A convergence study has been included in Ai and Augarde [57] where the adaptivity approach used showed better convergence properties than uniform refinement. Results using the CF in the two situations are presented in Tables 1 and 2 and all show good agreement with the analytical results in Eq. (24). It is clear that the results using different sizes of domains and contours are all accurate, indicating the integration of the CF and the J-integral are both path-independent, when the two parts of crack surface integration cancel out. The integration over a larger domain provides better accuracy, and the domain integration generally beats the contour integration. From Table 1, the contribution from crack surfaces to the CF is zero due to the symmetric stress field, while for another case it is not zero but much smaller than the result from the domain integration when a large domain is used. Using small domains, e.g. $c/a = 0.01$ and 0.001, the results appear unreasonable, which are caused by the oscillations around the crack tip (for instance, see the stresses along the crack surfaces in Fig. 6). For mode I fracture in Fig. 6(a), theoretical stresses along the crack surfaces are zero according to Eq. (24), however there are deviations for the results close to the crack tip. Even with a very fine particle distribution around the crack tip in this calculation, the accuracy for stresses within $r/a < 10^{-4}$ cannot be guaranteed due to the stress singularity at the crack tip, although in the range $r/a > 10^{-4}$ good accuracy can be achieved.

4.2. Single edge crack under tensile loading

The second example considers the propagation of a single crack in a slender plate under uniaxial tension (Fig. 7). The problem domain

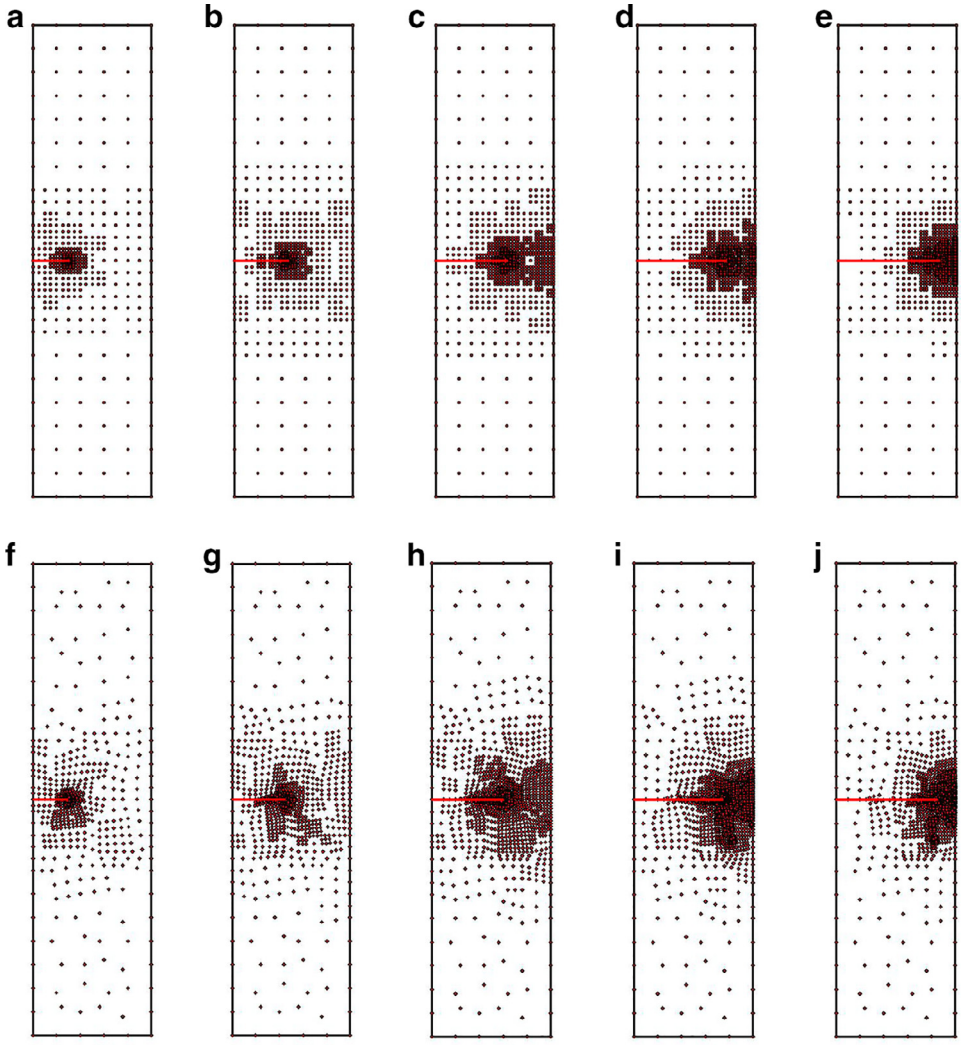

Fig. 8. Adaptive particle arrangements for the edge crack under uniaxial tension during propagation steps = 3, 6, 9, 12, 14 with different initial particle distributions: (a–e) case 1, (f–j) case 2.

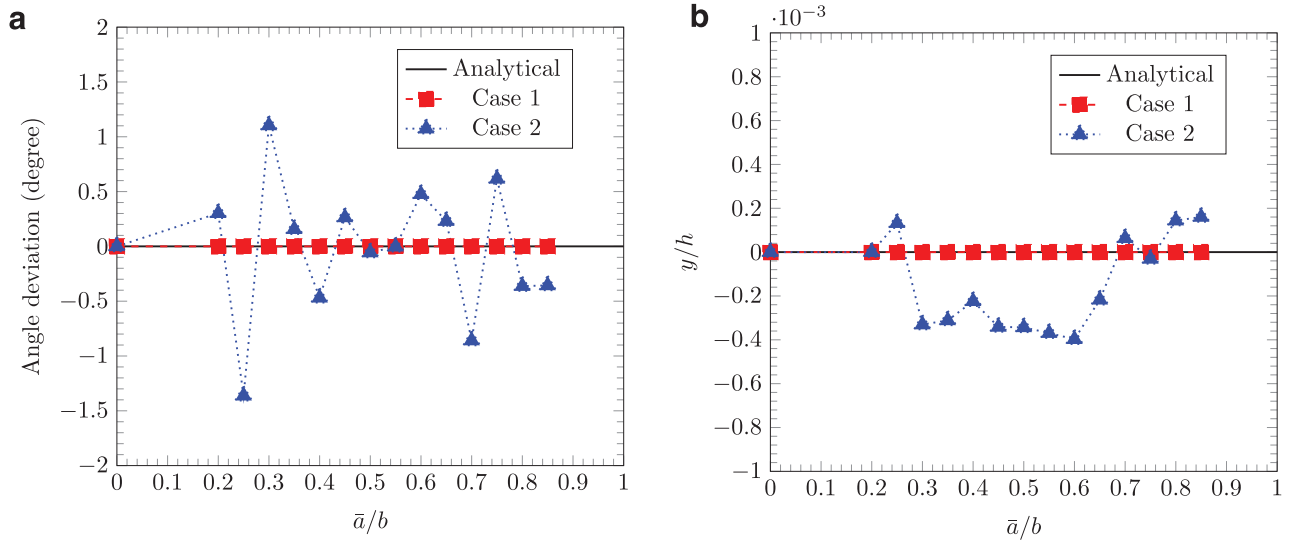

Fig. 9. Deviations for the edge crack propagation under uniaxial tension modelled by the configurational force: (a) angle in the local polar coordinates and (b) vertical location.

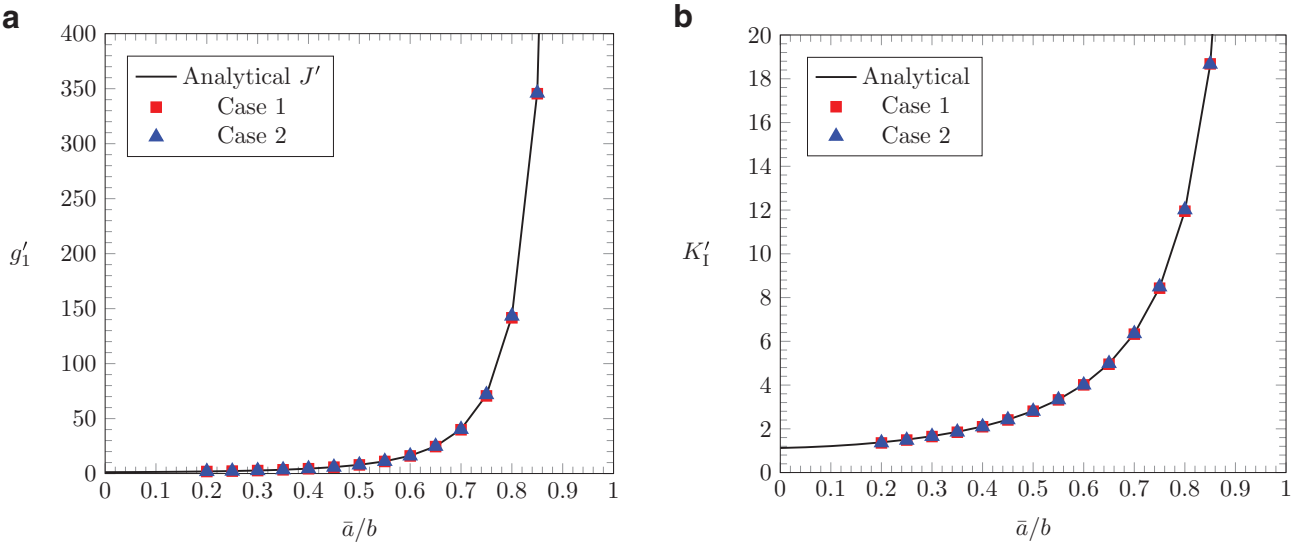

Fig. 10. Validation of results for the edge crack under uniaxial tension during crack propagation steps: (a) g_1' and (b) K_I'.

was discretised with either uniformly (case 1) or non-uniformly (case 2) distributed particles, as depicted in Fig. 7(b and c), to demonstrate the stability of the proposed method with different initial particle distributions. The geometry used was $a = 0.1$ m, $b = 5a$, $h = 10a$, $\eta_t = 0.02$, $da = a/4$ and tensile loading $\sigma = 10$ MPa on both upper and lower edges of the plate. Domain integration was used to calculate SIFs and the CF, where $c = 0.2a$ was applied. A plane strain condition was assumed and shear modulus $\mu = 80$ GPa and Poisson's ratio $\nu = 0.3$. The plate was fixed as in [28] by forcing the average displacements and rotations to zero. The analytical solution for the mode I SIF from [65] is

$$K_I/K_0 = 0.265(1 - \bar{a}/b)^4 + \frac{0.857 + 0.265\bar{a}/b}{(1 - \bar{a}/b)^{3/2}}, \tag{27}$$

where $K_0 = \sigma\sqrt{\pi\bar{a}}$ and $\bar{a}$ is the crack length after propagation.

Adaptive particle arrangements were generated during the crack propagation process and there was a "mass" of particles generated around the crack tip, as presented in Fig. 8. Due to the symmetry of the problem and initial particle distribution, particle arrangements in case 1 are symmetric and no deviation of crack direction from the central line during the crack propagation process, while for case 2 with asymmetric initial particle distribution, a slight deviation is found in the crack propagation as shown in Fig. 9. The crack propagation angle deviates way from zero for most of steps in Fig. 9(a), but the mean value remains close to zero and predicts a horizontal crack growth. Similar results can be found in [28]. The results for the mode I SIFs in both cases during all crack propagation steps show good agreement with the analytical values in Eq. (27), as shown in Fig. 10, where analytical g_1' is unknown but can be approximated by analytical J' using Eq. (21).

4.3. Single edge crack under shear loading

Mode II type crack propagation is included in the third example, where an edge crack in a square plate under shear loading, as depicted in Fig. 11, is used to compare the crack paths obtained by the CF approach (case 1) and by the MCSC (case 2). The plate has dimensions of $l = 1$ m and $a = 0.5l$, shear modulus $\mu = 8.0$ GPa and Poisson's ratio $\nu = 0.3$. For most crack propagation steps in case 1, the crack increment was set to $da = 0.05a$, except the first few steps in the CF case where the crack path changes its direction rapidly so a much smaller crack increment ($da = 0.01a$) was used. The target error for adaptivity was $\eta_t = 0.02$.

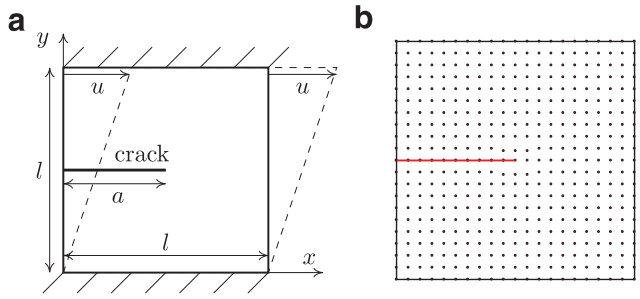

Fig. 11. Single edge crack under shear loading: (a) configuration and (b) initial particle distribution.

In case 2, a larger increment $da = 0.1a$ and target error $\eta_t = 0.04$ were used, and these parameters were also used for the CF approach to test their sensitivity on the results. The lower side of the plate was fixed and the upper side was horizontally shifted towards the left with $u = 0.02l$. Domain integration ($c = 0.01a$) was applied to obtain SIFs and the CF, where the integration over crack surfaces were excluded. A slight deviation of particles around the crack tip was applied, so the geometric antisymmetry of the problem was broken, to make sure the crack propagates to the lower side of the plate.

Adaptive particle arrangements for the crack propagation steps are given in Fig. 12. For the crack propagation led by the CF in case 1, the crack direction changes smoothly in Fig. 12(a and b) and then runs linearly towards the lower left corner, while the crack growth predicted by the MCSC has a rapid change in Fig. 12(e and f). A larger group of dense particles is generated at this kinked position (the centre of the plate) in the following propagation steps of case 2, comparing between Fig. 12(h) and (d). The CF approach thus provides a smooth transition for crack direction changes, while the MCSC allows a large kink in the crack growth, and again similar results can be found in Miehe et al. [27]. This difference can be explained from the theories of the two crack propagation criteria. Considering the initial crack, the deformation is under pure mode II so $K_I = 0$ and $K_{II} \neq 0$. The crack propagation angle given by the MCSC in Eq. (B.2) is $\theta = 70.5°$, while the CF is $g_1 \neq 0$ and $g_2 = 0$ using Eq. (21) and the CF is horizontally right. A comparison of the crack growths by the two approaches is given in Fig. 13, where the main difference occurs at the beginning propagation steps. It is notable that the crack path by the CF converges to the results given by the MCSC when more refinement

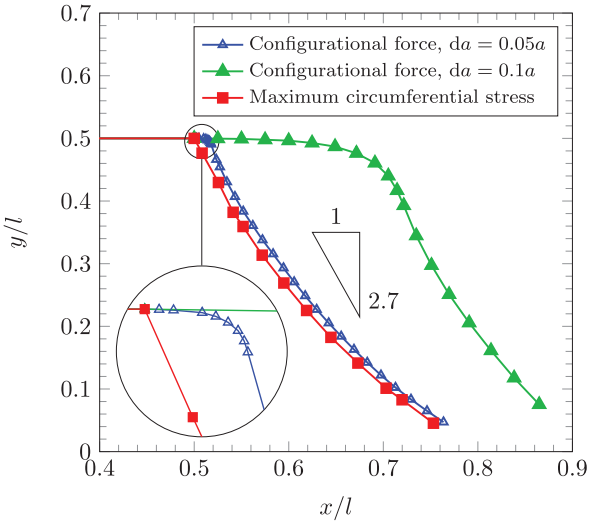

Fig. 13. A comparison of crack growth predictions under shear loading between by configurational force and by the maximum circumferential stress criterion.

steps and smaller crack increments are used. Similar final slopes are obtained by the two approaches, which are not far from the experimental results in [1] with the inclination angle around 70° ($\tan 70° \approx 2.7$).

4.4. Crack propagation in a cruciform plate

Mixed mode crack propagation is considered in the fourth example. A cruciform plate is placed under a uniform tensile loading ($\bar{t} = 100$ MPa) at the top and the other three sides are restricted in movement as shown in Fig. 14. The configuration is comprised of $L = 1$ m, $a = 0.2L$ and $\beta = 3\pi/4$, where a crack is located at the bottom-right corner of the plate. The initial particle arrangement is given in Fig. 14(b) and the adaptivity approach controls particle arrangements during the crack propagation steps with the target error $\eta_t = 0.04$. Adaptive particle arrangements are presented in Fig. 15, where fine particles are generated around the crack tip and three corners except the bottom-right. The final crack growth is presented in Fig. 16, where good agreements with the results by Prasad et al. [66] can be obtained. The values of the CF are compared with the SIFs in [66], and the satisfaction of Eq. (21) is achieved Fig. 16(b).

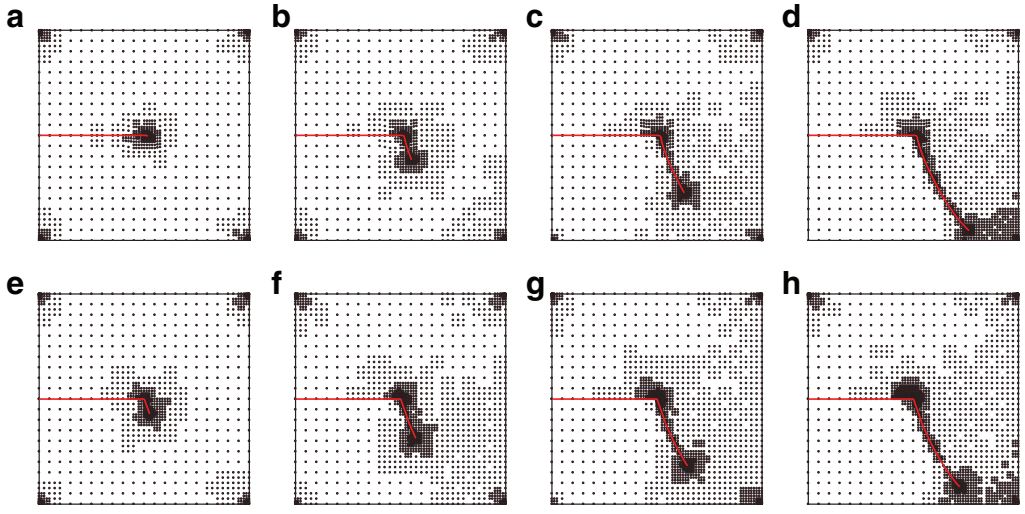

Fig. 12. Adaptive particle arrangements for the edge crack under shear loading during crack propagation steps: (a–d) steps = 7, 14, 21, 30 by configuration force; (e–h) steps = 3, 6, 9, 12 by maximum circumferential stress criterion.

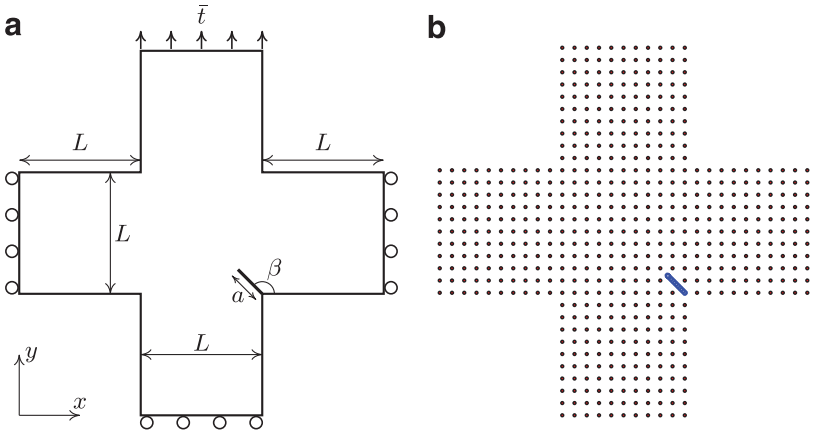

Fig. 14. Crack propagation in a cruciform plate under uniaxial tension: (a) configuration and (b) initial particles with cracking particles in blue. (For interpretation of the references to colour in this figure legend, the reader is referred to the web version of this article).

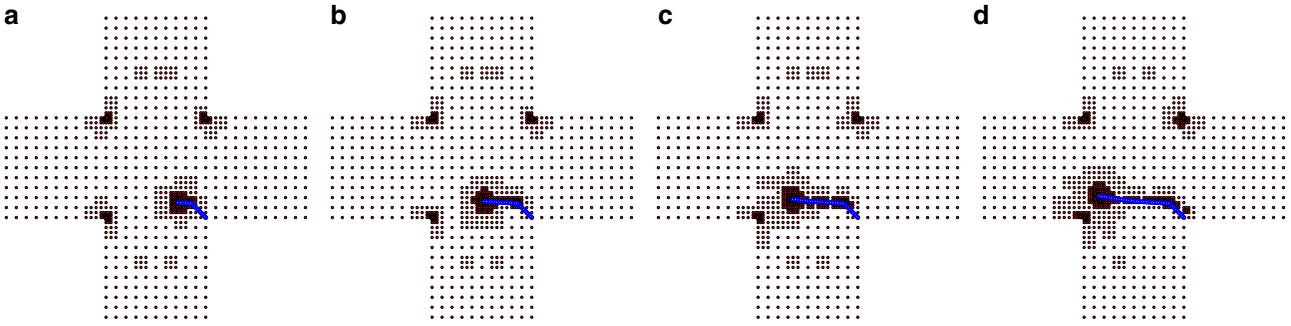

Fig. 15. Adaptive particle arrangements during crack propagation steps for the cruciform plate problem with cracking particles in blue: (a–d) step = 7, 15, 22 and 30. (For interpretation of the references to colour in this figure legend, the reader is referred to the web version of this article).

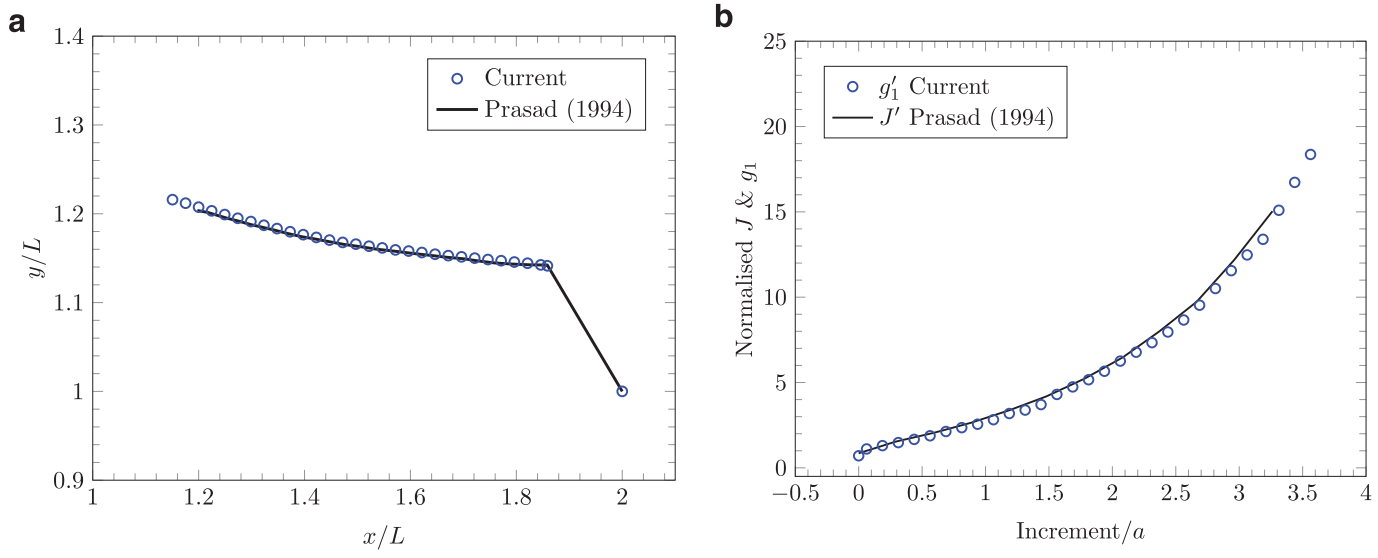

Fig. 16. Validation of the results for the cruciform plate problem: (a) crack growth and (b) normalised SIF and g_1.

4.5. Two cracks in a plate with two holes

The final example includes the propagation of two cracks, and the configuration is $L = 20$, $h = 10$, $a = 1$, $\mathrm{d}a = 0.5a$, $h_0 = 2.85$, $R = 2$ and $d = 3$ all with dimensions in mm (Fig. 17). The plate has a Young's modulus $E = 200$ GPa and a Poisson's ratio $\nu = 0.3$ and was loaded by fixing the bottom and vertically shifting the top edge by $u = 0.02h$. The target error is $\eta_t = 0.06$, which is a little higher than previous examples due to a more complex geometry. A square domain integration was used to calculate the CF (excluding the crack surface integration) with the size $c = 0.2a$ and also to execute the interaction integration for SIFs. Crack growth predicted by the CF is presented in Fig. 18, where the crack path predicted by the proposed method agrees with the results obtained by the MCSC in the CPM [51] and the polygon scaled boundary finite element method [67]. The CF component g_1 and the J-integral, J are normalised by Eq. (23) using $\sigma \approx 0.02E$. The

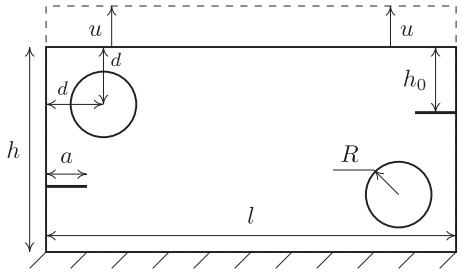

Fig. 17. Two cracks in a plate with two holes under uniaxial tension.

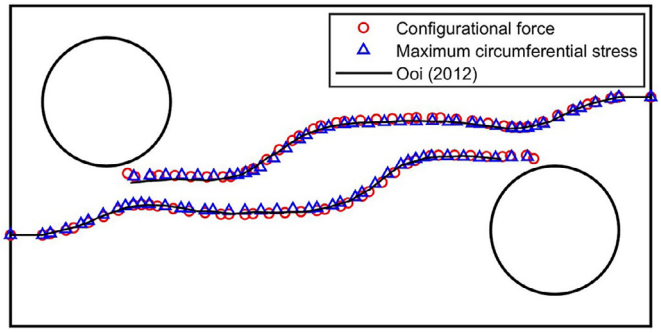

Fig. 18. Predicted crack propagation of two cracks driven by the configurational force and the maximum circumferential stress criterion.

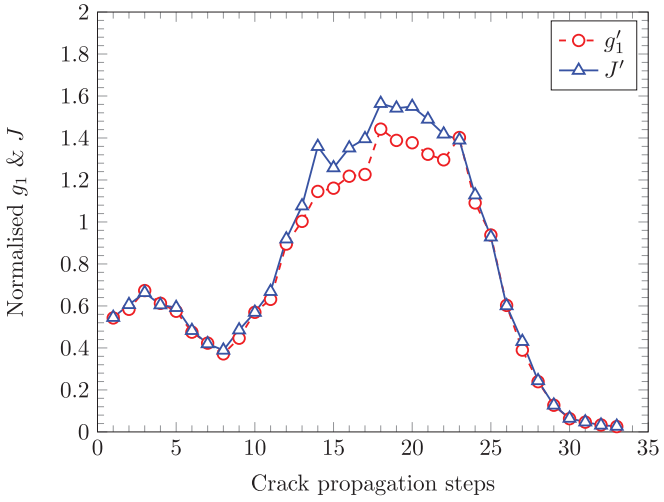

Fig. 19. Energy release rate during crack propagation steps for the two-crack problem.

comparison between g_1 and J during the crack propagation steps is given in Fig. 19, where good agreement is obtained between the two approaches, although little difference is found in steps 12–23. At these steps, the two crack tips become close to each other, which causes more complex stress distributions and leads to this difference.

5. Conclusions

A new configurational force driven cracking particle method has been developed for crack modelling in 2D, which can take the advantages of both the CF approach and the CPM. The crack propagation direction is directly provided by the CF, so there is no requirement to decompose the stress and displacement fields for mixed-mode fracture problems. The CPM uses a set of discontinuous crack segments to describe crack patterns, which reduces the complexity in problem approximation and is suitable for modelling multiple cracks. The CF can be calculated by contour integration or domain integration. Domain integration generally provides better accuracy than contour integration. The contribution from crack surfaces to the CF is much smaller than the value of the domain integration, and the result is affected by the error in the approximation around the crack tip, even with a very fine particle distribution. Comparing the modelling of crack propagation by the CF approach with the MCSC, the former gives a smooth change in crack direction, while the latter leads to a sudden change for the edge crack under shear loading. Both the CF approach and the MCSC can provide good predictions in crack propagation and the proposed method has shown its ability for modelling multiple crack propagation in the final example with two cracks. While we only present 2D problems in this paper, the key ideas can be transferred to 3D, where the full advantage of a meshless approach over a mesh-based approach will be realised

Acknowledgements

Financial support was received from the China Scholarship Council (CSC) during W. Ai's Ph.D., and from the UK EPSRC (grant EP/M507854/1) to support R.E. Bird's Ph.D. The authors acknowledge the support of the European Commission-funded RISE-project BESTOFRAC (734370). All data created during this research is openly available at doi:10.15128/r2wp988j83d/.

Appendix A. Adaptivity

The adaptivity procedure optimises the distribution of particles and is vital for crack problems in order to maintain the accuracy of results around the crack tip where there are high stress gradients. Reviews of different adaptivity approaches can be found in [51,68] and *a posteriori* adaptivity approach developed in [51] is introduced below.

The first step of the adaptivity approach is error estimation. The error of the results is estimated by a *recovery*-based error estimator [69] determined as

$$\|E_g\| = \left\{ \frac{1}{2} \int_\Omega (\boldsymbol{\sigma}^p - \boldsymbol{\sigma}^h)^{\mathrm{T}} \mathbf{D}^{-1} (\boldsymbol{\sigma}^p - \boldsymbol{\sigma}^h) \mathrm{d}\Omega \right\}^{\frac{1}{2}}, \tag{A.1}$$

where $\mathbf{D}$ is the material tangent stiffness, $\boldsymbol{\sigma}^p$ and $\boldsymbol{\sigma}^h$ are the projected stress and the calculated stress, respectively, written in Voigt notation, e.g. $\boldsymbol{\sigma}^h = [\sigma^h_{11}, \sigma^h_{22}, \sigma^h_{12}]$. $\boldsymbol{\sigma}^p$ is a projection of the exact stress which is unknown for many problems and is therefore instead obtained as

$$\boldsymbol{\sigma}^p = \sum_{k=1}^{m} \Psi_k(\mathbf{x}) \boldsymbol{\sigma}^h(\mathbf{x}_k), \tag{A.2}$$

where m is the number of surrounding particles with supports covering $\mathbf{x}$, and $\Psi_k(\mathbf{x})$ is a shape function from the MLS approximation using smaller supports. The global error η_g for the problem domain is evaluated by

$$\eta_g = \frac{\|E_g\|}{\|U\|}, \tag{A.3}$$

with

$$\|U\| = \left\{ \frac{1}{2} \int_\Omega (\boldsymbol{\sigma}^h)^{\mathrm{T}} \mathbf{D}^{-1} \boldsymbol{\sigma}^h \mathrm{d}\Omega \right\}^{1/2}. \tag{A.4}$$

A target error η_t is predefined by the user according to the accuracy requirement of problems, and when $\eta_g > \eta_t$, the adaptivity process is applied.

Then refinement of particles is executed in the local zone with large errors. For the ith cell, the local error is estimated by replacing the global domain Ω in Eq. (A.1) with the cell area Ω_i, as

$$\|E_i\| = \left\{ \frac{1}{2} \int_{\Omega_i} (\boldsymbol{\sigma}^p - \boldsymbol{\sigma}^h)^{\mathrm{T}} \mathbf{D}^{-1} (\boldsymbol{\sigma}^p - \boldsymbol{\sigma}^h) \mathrm{d}\Omega_i \right\}^{\frac{1}{2}}. \tag{A.5}$$

The relative local error is obtained by taking the global error into account, as

$$\eta_i = \frac{\|E_i\|}{\|U\|/\sqrt{n_{\text{cell}}}}, \tag{A.6}$$

where n_{cell} is the total number of background cells. When η_i is larger than the refinement threshold L_{fin}, cell i is divided to four small cells following a quad-tree structure and five particles are added; when four small cells have lower errors than the coarsening threshold L_{rec}, they are combined to a large cell and five particles are deleted, as

$$\begin{cases} \eta_i > L_{\text{fin}} & \text{to be refined}, \\ \eta_i < L_{\text{rec}} & \text{to be coarsened}. \end{cases} \tag{A.7}$$

L_{fin} and L_{rec} are determined by a relationship with the target global error η_{t}

$$L_{\text{fin}} = 2\eta_{\text{t}}, \quad L_{\text{rec}} = 0.5\eta_{\text{t}}. \tag{A.8}$$

Appendix B. Maximum circumferential stress criterion (MCSC)

The MCSC has been widely used for modelling crack propagation, e.g. [4,9,51]. In the MCSC, crack propagation is towards the direction where the shear stress $\sigma_{r\theta}$ at the crack tip becomes zero, i.e.

$$\sigma_{r\theta} = \frac{\cos\frac{\theta}{2}}{2\pi r}\left[\frac{K_{\text{I}}\sin(\theta)}{2} + \frac{K_{\text{II}}(3\cos(\theta)-1)}{2}\right] = 0. \tag{B.1}$$

Here $\sigma_{r\theta}$ is achieved using SIFs to avoid the issue of singular stresses at the crack tip. The solution is

$$\theta = 2\arctan\left(\frac{K_{\text{I}} - \sqrt{K_{\text{I}}^2 + 8K_{\text{II}}^2}}{4K_{\text{II}}}\right), \tag{B.2}$$

where θ is the angle for the crack increment in the local polar coordinate system at the crack tip.

Appendix C. Interaction integration

The interaction integral is based on the J-integral and used to obtain SIFs for mixed mode fracture [70]. The domain form of the J-integral in 2D is

$$J = \int_A \left(\sigma_{ij}u_{j,1} - W\delta_{1i}\right)q_{,i}\mathrm{d}A, \quad i,j \in \{1,2\}, \tag{C.1}$$

where W is the strain energy as in Eq. (5), q is a weight function as in Eq. (22) and δ is the Kronecker delta function. $q_{,i}$ stands for the derivative of q to x_i, i.e. $\partial q/\partial x_i$. Considering two equilibrium states, a real state (state 1) and an auxiliary state (state 2), the superposition for the J-integral is

$$J^{(1+2)} = J^{(1)} + J^{(2)} + I^{(1,2)}, \tag{C.2}$$

and the interaction integral is

$$I^{(1,2)} = \int_A \left(\sigma_{ij}^{(1)}u_{j,1}^{(2)} + \sigma_{ij}^{(2)}u_{j,1}^{(1)} - W^{(1,2)}\delta_{1i}\right)q_{,i}\mathrm{d}A, \tag{C.3}$$

where the superscripts (1) and (2) indicate the terms from states 1 and 2, respectively, and the interaction strain energy is $W^{(1,2)} = \sigma_{ij}^{(1)}\varepsilon_{ij}^{(2)} = \sigma_{ij}^{(2)}\varepsilon_{ij}^{(1)}$. The relationship between the interaction integral and the SIFs is obtained from Eq. (C.2), as

$$I^{(1,2)} = 2\alpha(K_{\text{I}}^{(1)}K_{\text{I}}^{(2)} + K_{\text{II}}^{(1)}K_{\text{II}}^{(2)}). \tag{C.4}$$

For mixed mode fracture, SIFs are obtained in two steps with selecting the specific auxiliary state, e.g. with $K_{\text{I}}^{(2)} = 1$ and $K_{\text{II}}^{(2)} = 0$, mode I SIF is obtained by $K_{\text{I}} = I^{(1,2)}/(2\alpha)$; and using $K_{\text{II}}^{(2)} = 1$ and $K_{\text{I}}^{(2)} = 0$, mode II SIF is $K_{\text{II}} = I^{(1,2)}/(2\alpha)$. The auxiliary field is defined as

$$\sigma_{11}^{(2)} = \frac{1}{\sqrt{2\pi r}}\left[K_{\text{I}}^{(2)}\cos\frac{\theta}{2}\left(1-\sin\frac{\theta}{2}\sin\frac{3\theta}{2}\right) - K_{\text{II}}^{(2)}\sin\frac{\theta}{2}\left(2+\cos\frac{\theta}{2}\cos\frac{3\theta}{2}\right)\right], \tag{C.5a}$$

$$\sigma_{22}^{(2)} = \frac{1}{\sqrt{2\pi r}}\left[K_{\text{I}}^{(2)}\cos\frac{\theta}{2}\left(1+\sin\frac{\theta}{2}\sin\frac{3\theta}{2}\right) + K_{\text{II}}^{(2)}\sin\frac{\theta}{2}\cos\frac{\theta}{2}\cos\frac{3\theta}{2}\right], \tag{C.5b}$$

$$\sigma_{12}^{(2)} = \frac{1}{\sqrt{2\pi r}}\left[K_{\text{I}}^{(2)}\sin\frac{\theta}{2}\cos\frac{\theta}{2}\cos\frac{3\theta}{2} + K_{\text{II}}^{(2)}\cos\frac{\theta}{2}\left(1-\sin\frac{\theta}{2}\sin\frac{3\theta}{2}\right)\right], \tag{C.5c}$$

$$u_1^{(2)} = \frac{1}{2\mu}\sqrt{\frac{r}{2\pi}}\left[K_{\text{I}}^{(2)}\cos\frac{\theta}{2}\left(\kappa-1+2\sin^2\frac{\theta}{2}\right) + K_{\text{II}}^{(2)}\sin\frac{\theta}{2}\left(\kappa+1+2\cos^2\frac{\theta}{2}\right)\right], \tag{C.5d}$$

$$u_2^{(2)} = \frac{1}{2\mu}\sqrt{\frac{r}{2\pi}}\left[K_{\text{I}}^{(2)}\sin\frac{\theta}{2}\left(\kappa+1-2\cos^2\frac{\theta}{2}\right) - K_{\text{II}}^{(2)}\cos\frac{\theta}{2}\left(\kappa-1-2sin^2\frac{\theta}{2}\right)\right], \tag{C.5e}$$

where μ is the shear modulus and κ is the Kolosov constant, which is defined as

$$\kappa = \begin{cases} 3-4\nu, & \text{plane strain}, \\ \dfrac{3-\nu}{1+\nu}, & \text{plane stress}. \end{cases} \tag{C.6}$$

The auxiliary strains are

$$\varepsilon_{11}^{(2)} = \frac{\partial u_1^{(2)}}{\partial x_1}, \quad \varepsilon_{22}^{(2)} = \frac{\partial u_2^{(2)}}{\partial x_2}, \quad \varepsilon_{12}^{(2)} = \frac{1}{2}\left(\frac{\partial u_2^{(2)}}{\partial x_1} + \frac{\partial u_1^{(2)}}{\partial x_2}\right). \tag{C.7}$$

References

[1] Erdogan F, Sih G. On the crack extension in plates under plane loading and transverse shear. J Fluids Eng 1963;85(4):519–25.
[2] Sih G, Macdonald B. Fracture mechanics applied to engineering problems-strain energy density fracture criterion. Eng Fract Mech 1974;6(2):361–86.
[3] Wu C-H. Fracture under combined loads by maximum-energy-release-rate criterion. J Appl Mech 1978;45(3):553–8.
[4] Belytschko T, Black T. Elastic crack growth in finite elements with minimal remeshing. Int J Numer Methods Eng 1999;45(5):601–20.
[5] Dolbow J, Belytschko T. A finite element method for crack growth without remeshing. Int J Numer Methods Eng 1999;46(1):131–50.
[6] Duflot M, Nguyen-Dang H. A meshless method with enriched weight functions for fatigue crack growth. Int J Numer Methods Eng 2004;59(14):1945–61.
[7] Zhuang X, Augarde C, Bordas S. Accurate fracture modelling using meshless methods, the visibility criterion and level sets: formulation and 2D modelling. Int J Numer Methods Eng 2011;86(2):249–68.
[8] Dai S, Augarde C, Du C, Chen D. A fully automatic polygon scaled boundary finite element method for modelling crack propagation. Eng Fract Mech 2015;133:163–78.
[9] Bouchard PO, Bay F, Chastel Y. Numerical modelling of crack propagation: automatic remeshing and comparison of different criteria. Comput Methods Appl Mech Eng 2003;192(35):3887–908.
[10] Richard H, Fulland M, Sander M. Theoretical crack path prediction. Fatigue Fract Eng Mater Struct 2005;28(1–2):3–12.
[11] Eshelby JD. The force on an elastic singularity. Philos Trans R Soc A – Math Phys Eng Sci 1951;244(877):87–112.
[12] Maugin GA. Material forces: concepts and applications. Appl Mech Rev 1995;48(5):213–45.
[13] Gurtin ME, Podio-Guidugli P. Configurational forces and the basic laws for crack propagation. J Mech Phys Solids 1996;44(6):905–27.
[14] Miehe C, Gürses E. A robust algorithm for configurational-force-driven brittle crack propagation with R-adaptive mesh alignment. Int J Numer Methods Eng 2007;72(2):127–55.
[15] Maugin G, Trimarco C. Pseudomomentum and material forces in nonlinear elasticity: variational formulations and application to brittle fracture. Acta Mech 1992;94(1–2):1–28.
[16] Steinmann P, Ackermann D, Barth F. Application of material forces to hyperelastostatic fracture mechanics. II. Computational setting. Int J Solids Struct 2001;38(32–33):5509–26.
[17] Mueller R, Maugin G. On material forces and finite element discretizations. Comput Mech 2002;29(1):52–60.
[18] Mueller R, Kolling S, Gross D. On configurational forces in the context of the finite element method. Int J Numer Methods Eng 2002;53(7):1557–74.
[19] Heintz P. On the numerical modelling of quasi-static crack growth in linear elastic fracture mechanics. Int J Numer Methods Eng 2006;65(2):174–89.

[20] Simha N, Fischer F, Shan G, Chen C, Kolednik O. J-integral and crack driving force in elastic–plastic materials. J Mech Phys Solids 2008;56(9):2876–95.
[21] Özenç K, Kaliske M, Lin G, Bhashyam G. Evaluation of energy contributions in elasto-plastic fracture: a review of the configurational force approach. Eng Fract Mech 2014;115:137–53.
[22] Kaczmarczyk Ł, Nezhad MM, Pearce C. Three-dimensional brittle fracture: configurational-force-driven crack propagation. Int J Numer Methods Eng 2014;97(7):531–50.
[23] Ballarini R, Royer-Carfagni G. A Newtonian interpretation of configurational forces on dislocations and cracks. J Mech Phys Solids 2016;95:602–20.
[24] Kuhn C, Lohkamp R, Schneider F, Aurich JC, Mueller R. Finite element computation of discrete configurational forces in crystal plasticity. Int J Solids Struct 2015;56:62–77.
[25] Özenç K, Chinaryan G, Kaliske M. A configurational force approach to model the branching phenomenon in dynamic brittle fracture. Eng Fract Mech 2016;157:26–42.
[26] Maugin GA. Configurational forces: thermomechanics, physics, mathematics, and numerics. Chapman and Hall/CRC; 2016.
[27] Miehe C, Gürses E, Birkle M. A computational framework of configurational–force-driven brittle fracture based on incremental energy minimization. Int J Fract 2007;145(4):245–59.
[28] Bird R, Coombs W, Giani S. A quasi-static discontinuous Galerkin configurational force crack propagation method for brittle materials. Int J Numer Methods Eng 2018;113(7):1061–80.
[29] Belytschko T, Lu Y, Gu L. Element-free Galerkin methods. Int J Numer Methods Eng 1994;37(2):229–56.
[30] Liu WK, Jun S, Zhang YF. Reproducing kernel particle methods. Int J Numer Methods Fluids 1995;20(8–9):1081–106.
[31] Atluri SN, Zhu T. A new meshless local Petrov–Galerkin (MLPG) approach in computational mechanics. Comput Mech 1998;22(2):117–27.
[32] Franke C, Schaback R. Solving partial differential equations by collocation using radial basis functions. Appl Math Comput 1998;93(1):73–82.
[33] Fan L, Coombs WM, Augarde CE. The point collocation method with a local maximum entropy approach. Comput Struct 2018;201:1–14.
[34] Belytschko T, Krongauz Y, Organ D, Fleming M, Krysl P. Meshless methods: an overview and recent developments. Comput Methods Appl Mech Eng 1996;139(1):3–47.
[35] Nguyen VP, Rabczuk T, Bordas S, Duflot M. Meshless methods: a review and computer implementation aspects. Math Comput Simul 2008;79(3):763–813.
[36] Chen JS, Hillman M, Chi S. Meshfree methods: progress made after 20 years. J Eng Mech 2017;143(4):04017001.
[37] Tian R, Wen L. Improved XFEM – an extra-DOF free, well-conditioning, and interpolating XFEM. Comput Methods Appl Mech Eng 2015;285:639–58.
[38] Zhuang X, Augarde C, Mathisen K. Fracture modeling using meshless methods and level sets in 3D: framework and modeling. Int J Numer Methods Eng 2012a;92(11):969–98.
[39] Silling SA, Askari E. A meshfree method based on the peridynamic model of solid mechanics. Comput Struct 2005;83(17):1526–35.
[40] Ma G, An X, Zhang H, Li L. Modeling complex crack problems using the numerical manifold method. Int J Fract 2009;156(1):21–35.
[41] Zheng H, Liu F, Li C. The MLS-based numerical manifold method with applications to crack analysis. Int J Fract 2014;190(1–2):147–66.
[42] Karma A, Kessler DA, Levine H. Phase-field model of mode iii dynamic fracture. Phys Rev Lett 2001;87(4):045501.
[43] Miehe C, Welschinger F, Hofacker M. Thermodynamically consistent phase-field models of fracture: variational principles and multi-field FE implementations. Int J Numer Methods Eng 2010;83(10):1273–311.
[44] Rabczuk T, Belytschko T. Cracking particles: a simplified meshfree method for arbitrary evolving cracks. Int J Numer Methods Eng 2004;61(13):2316–43.
[45] Rabczuk T, Bordas S, Zi G. A three-dimensional meshfree method for continuous multiple-crack initiation, propagation and junction in statics and dynamics. Comput Mech 2007a;40(3):473–95.
[46] Ren H, Zhuang X, Cai Y, Rabczuk T. Dual-horizon peridynamics. Int J Numer Methods Eng 2016;108(12):1451–76.
[47] Ren H, Zhuang X, Rabczuk T. Dual-horizon peridynamics: a stable solution to varying horizons. Comput Methods Appl Mech Eng 2017;318:762–82.
[48] Amiri F, Millán D, Shen Y, Rabczuk T, Arroyo M. Phase-field modeling of fracture in linear thin shells. Theor Appl Fract Mech 2014;69:102–9.
[49] Rabczuk T, Belytschko T. Application of particle methods to static fracture of reinforced concrete structures. Int J Fract 2006;137(1–4):19–49.
[50] Rabczuk T, Zi G, Bordas S, Nguyen-Xuan H. A simple and robust three-dimensional cracking-particle method without enrichment. Comput Methods Appl Mech Eng 2010;199(37):2437–55.
[51] Ai W, Augarde CE. An adaptive cracking particle method for 2D crack propagation. Int J Numer Methods Eng 2016;108(13):1626–48.
[52] Ai W, Augarde CE. An adaptive cracking particle method providing explicit and accurate description of 3D crack surfaces. Int J Numer Methods Eng 2018a;114:1291–309.
[53] Kumar V, Ghosh A. Modeling of dynamic fracture based on the cracking particles method. Theor Appl Fract Mech 2015;75:22–31.
[54] Chen L, Zhang Y. Dynamic fracture analysis using discrete cohesive crack method. Int J Numer Methods Biomed 2010;26(11):1493–502.
[55] Kumar V, Drathi R. A meshless cracking particles approach for ductile fracture. KSCE J Civ Eng 2014;18(1):238–48.
[56] Rabczuk T, Areias P, Belytschko T. A simplified mesh-free method for shear bands with cohesive surfaces. Int J Numer Methods Eng 2007b;69(5):993–1021.
[57] Ai W, Augarde CE. A multi-cracked particle method for complex fracture problems in 2D. Math Comput Simul 2018b;150:1–24.
[58] Zhuang X, Heaney C, Augarde C. On error control in the element-free Galerkin method. Eng Anal Boundary Elem 2012b;36(3):351–60.
[59] Dolbow J, Belytschko T. An introduction to programming the meshless element free Galerkin method. Arch Comput Methods Eng 1998;5(3):207–41.
[60] Rabczuk T, Belytschko T. A three-dimensional large deformation meshfree method for arbitrary evolving cracks. Comput Methods Appl Mech Eng 2007;196(29):2777–99.
[61] Podio-Guidugli P. Configurational forces: are they needed? Mech Res Commun 2002;29(6):513–19.
[62] Heintz P, Larsson F, Hansbo P, Runesson K. Adaptive strategies and error control for computing material forces in fracture mechanics. Int J Numer Methods Eng 2004;60(7):1287–99.
[63] Schütte H, Molla-Abbasi K. On a numerical scheme for curved crack propagation based on configurational forces and maximum dissipation. In: Proceedings in applied mathematics and mechanics, Vol. 8. Wiley Online Library; 2008. p. 10239–40.
[64] Westergaard HM. Bearing pressures and cracks. J Appl Mech 1939;6(2):A49–53.
[65] Tada H, Paris P, Irwin G. The analysis of cracks handbook. New York: ASME Press; 2000.
[66] Prasad N, Aliabadi M, Rooke D. Incremental crack growth in thermoelastic problems. Int J Fract 1994;66(3):R45–50.
[67] Ooi ET, Song C, Tin-Loi F, Yang Z. Polygon scaled boundary finite elements for crack propagation modelling. Int J Numer Methods Eng 2012;91(3):319–42.
[68] Lee CK, Zhou C. On error estimation and adaptive refinement for element free Galerkin method. Part I: stress recovery and a posteriori error estimation. Comput Struct 2004;82(4):413–28.
[69] Chung H, Belytschko T. An error estimate in the EFG method. Comput Mech 1998;21(2):91–100.
[70] Yau J, Wang S, Corten H. A mixed-mode crack analysis of isotropic solids using conservation laws of elasticity. J Appl Mech 1980;47(2):335–41.